

# Observing the Sun: from start to finish.

PhD dissertation by

**Pablo Santamarina Guerrero**

Instituto de Astrofísica de Andalucía (IAA-CSIC)

Programa de Doctorado en Física y Matemáticas (FisyMat)  
Universidad de Granada

A thesis submitted in fulfillment  
of the requirements of the degree of  
Doctor of Philosophy

June 13, 2024

PhD thesis supervised by

**Dr. David Orozco Suárez**

**Dr. Julián Blanco Rodríguez**



**UNIVERSIDAD  
DE GRANADA**



# ACKNOWLEDGEMENTS

Agradecimientos



# RESUMEN

Resumen de la tesis



# SUMMARY

Summary of the thesis





# CONTENTS

<b>1</b>	<b>Introduction</b>	<b>1</b>
1.1	Background . . . . .	1
1.2	Motivation of our work . . . . .	2
1.3	Introduction . . . . .	3
<b>2</b>	<b>TuMag’s design and calibration.</b>	<b>5</b>
2.1	A brief introduction to spectropolarimeters. . . . .	5
2.1.1	Spectroscopy . . . . .	6
2.1.2	Imaging . . . . .	8
2.1.3	Polarimetry . . . . .	8
2.2	The Tunable magnetograph: TuMag . . . . .	8
2.2.1	Optical design and image quality. . . . .	8
2.2.2	Spectral capabilities . . . . .	8
2.2.3	Polarimetric capabilities . . . . .	8
2.3	Calibration of TuMag . . . . .	8
<b>3</b>	<b>Operation and data reduction.</b>	<b>9</b>
3.1	TuMag’s Observation modes and data reduction. Data’s pipeline. . . . .	9
<b>4</b>	<b>Challenges in data reduction: Etalon Cavity Map.</b>	<b>11</b>
4.1	Cavity map retrieval from flat-field observations . . . . .	11
4.1.1	One device, two configurations . . . . .	11
4.1.1.1	Collimated configuration . . . . .	11
4.1.1.2	Telecentric configuration . . . . .	12
<b>5</b>	<b>Scientific exploitation.</b>	<b>13</b>
5.1	Persistent Homology in Solar Magnetograms. . . . .	13
5.1.1	Persistent Homology . . . . .	13
5.1.2	Persistent Images . . . . .	16
5.1.3	Data . . . . .	18
5.1.3.1	Quiet Sun observations . . . . .	18
5.1.3.2	Active regions observations . . . . .	18
5.1.3.3	Analysis and results . . . . .	19
5.1.3.4	Quiet Sun results . . . . .	22

---

5.1.3.5	Active region results . . . . .	24
5.1.3.6	‘Interacting’ Diagram . . . . .	27
5.1.3.7	Conclusions . . . . .	29
<b>6</b>	<b>Summary and conclusions</b>	<b>31</b>
<b>A</b>	<b>Profile derivatvies</b>	<b>33</b>

# CHAPTER 1

---

## INTRODUCTION

### 1.1 Background

In June 2009, the first Sunrise observatory (Barthol et al., 2011) was launched from Kiruna, Sweden, aboard a stratospheric balloon. Equipped with a 1-m aperture telescope, a multi-wavelength UV filter imager, and IMaX, a Fabry-Pérot-based magnetograph, Sunrise was the most complex payload carried by a solar stratospheric balloon to date. Aimed at studying the magnetic fields of the Sun and the dynamics of solar plasma convective flows, the mission was an outstanding success. It resulted in the publication of over a hundred peer-reviewed scientific articles in numerous high-impact journals, including *Astronomy and Astrophysics* (A&A), *The Astrophysical Journal* (APJ), and *Solar Physics*, among others.

Following the success of its inaugural flight, Sunrise embarked on a second journey (Solanki et al., 2017) on June 13, 2013. The primary objective of this subsequent flight was to investigate the active regions of the Sun, as it remained completely \*quiet\* throughout the entirety of the initial flight. Despite minimal alterations to the instrumentation aboard the observatory, the variance in solar activity during this second flight yielded fresh perspectives and valuable data, ultimately securing the mission success, despite encountering some technical challenges.

Given the success of the first two flights, a third iteration of the Sunrise mission was planned, featuring an updated design. For this third edition, the telescope was equipped with three post-focal instruments: SUSI, a UV spectrograph; SCIP, an infrared spectrograph; and TuMag, the evolution of the IMaX magnetograph. Sunrise III was initially scheduled to fly during the summer of 2020 but was postponed to 2022.

The third launch of Sunrise plays a crucial role in this dissertation. This thesis, initiated in 2020, was centered on the development of the data reduction pipeline for the TuMag instrument, which was entirely developed by the Spanish solar physics consortium. According to the original plan, the first half of the thesis was dedicated to the calibration of the instrument and the preparation of the data pipeline. This way, once the mission was launched, the second half of the thesis could focus on the correction and scientific analysis of the data produced during this third flight. However, this plan (and thus the scope of the thesis) encountered a setback on July 10, 2022, when the third flight of the Sunrise observatory had to be aborted just a few hours after the launch due to a mechanical failure during

the ascent phase.

The observatory was recovered days later after a brief stay in the Scandinavian Alps. Both the telescope and the instruments were found to be in good condition, allowing for the recovery of the observatory and providing hope for a second attempt. However, the process of retrieving the instruments, disassembling, calibrating, and verifying their condition before relaunching the mission is lengthy, and it was not until this year, 2024, that a second attempt became feasible.

In the absence of data produced by Sunrise to process, analyze, and exploit, the scientific work conducted within the framework of this thesis has been compelled to slightly shift its focus. Over these years, we have focused on delving deeper into image correction techniques for data obtained from Fabry-Pérot interferometers, such as TuMag and IMaX. As well as conducting several studies using data products from other instruments, such as the Polarimetric and Helioseismic Imager aboard Solar Orbiter (SO/PHI) and HMI.

In the following chapters, we will present the work undertaken during the calibration and commissioning of TuMag, conducted in 2021, 2022, and 2024. Additionally, the research carried out between the first and second flights of Sunrise III, which has resulted in the publication of two articles as the main author — one published in APJ and the other in A&A — will also be detailed in this manuscript, as well as other studies that have not yet been published in any scientific journal.

## 1.2 Motivation of our work

In experimental sciences, there is a very strong relation between technological and scientific advances due to the simple fact that we cannot draw conclusions from what we cannot see. We believe it is important for experimental scientists, and more specifically, for observational astronomers, to know the limitations and capabilities and understand the functioning of the instruments we use.

This philosophy is one of the pillars of this thesis, which covers topics ranging from the design and calibration of scientific instruments to the exploitation of the data they produce. With this thesis, we aim to provide a broad, yet detailed, view of the various stages of a scientific mission, from its conception and objectives through its design and calibration, data reduction and preparation for scientific exploitation, and finally, the studies and conclusions derived from it.

In particular, we will detail this process within the framework of solar physics through the development of TuMag, the magnetograph aboard Sunrise III. We will present the scientific objectives of the mission and attempt to link the design concepts with the scientific questions we aim to answer. We will address the challenges encountered in data correction due to the technical or instrumental limitations, a subject of ongoing debate within the community and of current relevance. And finally, we also aim to offer a brief dip into the scientific exploitation that can be carried out with the final data product.

With this thesis we aim to clarify the following points:

- ✱ Scientific objectives of TuMag.

- ✱ Instrumental ways of achieving the scientific purposes
- ✱ Open problems for data reduction. Flat-fields, etalon effects in the data.
- ✱ Offering an example of data exploitation with aa study case. Persistent Homology.

## 1.3 Introduction

Astronomy is one of the broadest fields of knowledge. It studies everything from the smallest (astronomically speaking) objects, such as the small asteroids that inhabit our solar system, to the global structure and evolution of the universe, including the study of planetary systems, stars, black holes and the galaxies in which they are found. However, despite the diversity of disciplines—ranging from stellar astronomy, radio astronomy, and cosmology, to extragalactic astronomy, astrobiology, and solar physics—they all share a common tool for studying the cosmos: light. Since the very beginning of astronomy, the astronomer’s work has been to learn how to modify and measure the properties of the photons that reach us in order to infer the characteristics of the observed object. Although recent advancements have provided astronomers with new lenses to see the cosmos, like gravitational waves (**REFERENCIA**) or neutrinos (**REFERENCIA**), among others, light remains as our main resource. Our understanding of the cosmos has always gone hand-in-hand with our ability to design and develop new ways (or more efficient ways) to dissect the light, spanning from the first solar clocks or Newton’s first telescope to the modern-day spaceborne telescopes like the Hubble, James Webb or Solar Orbiter.

Solar physics is no different from other astronomical disciplines in this regard. Our main tool to *see* the Sun is through light. Contrary to what one may think, solar physicists are as photon-starved as any other astronomer. Even though our star is closer and (apparently) brighter than any other astronomical object, our requirements regarding resolution and sensitivity are so high we are as dependent on extremely optimized instrumentation as any other discipline. Thus, the development of instrumentation employing state-of-the-art technology and techniques plays an important role in modern solar physics.



## CHAPTER 2

---

# TuMAG'S DESIGN AND CALIBRATION.

In this chapter we take the first steps of the journey of developing an instrument to observe the Sun. We will define...

The SUNRISE III mission aims to study and establish the relations and couplings between the phenomena occurring at different layers of the Sun's surface. With this purpose in mind, three different post-focal instruments were included in the design, each of them responsible of observing at different regions of the spectrum. The SUNRISE UV Spectropolarimeter and Imager (SUSI, **REFERENCIA**), which will observe the spectra between 309 nm and 417 nm; The Sunrise Chromospheric Infrared spectroPolarimeter (SCIP, **REFERENCIA**), which will observe the near-infrared; and lastly, the Tunable Magnetograph (TuMag), which will observe three spectral lines in the visible, at 525.02 nm, 525.06 nm and 517 nm.

The design from scratch of an instrument such as this is very complex. There are many things that have to be meticulously designed and tested which span many fields of expertise, like optics, electronics, software, hardware, or thermal design. To avoid undue extension of this thesis, we will focus on the aspects of the design directly related to the **TO QUE**, that is, regarding the spectral, imaging and polarimetric capabilities of the instrument.

### 2.1 A brief introduction to spectropolarimeters.

Spectropolarimeters, as suggested by the name, are devices that measure the spectral and polarimetric properties of light, or in other words, that measure the polarization state of light as a function of wavelength. Their use is widely extended in astrophysics due to the huge amount of information about the light source we can infer from these properties.

In solar physics, it is common to encounter two distinct types of spectropolarimeters, distinguished by their approach to spectroscopy: slit-based spectrographs, such as SUSI and SCIP, and narrow-band tunable filtergraphs, like TuMag. The latter preserve spatial resolution by capturing two-dimensional images of the solar scene at the expense of sacrificing spectral resolution. Conversely, slit-based spectrographs provide excellent spectral resolution but have a limited spatial resolution.

Regardless of how spectroscopy is carried out, spectropolarimeters must be able to measure the polarization state of light. That is, they must be capable of determining the Stokes

parameters of the incident light. These four parameters, usually grouped in a pseudo-vector:  $[I, Q, U, V]$ , were defined by Stokes in Stokes (1851) as a mathematical formalism to completely define the polarization state of light. The first parameter,  $I$ , represents the total intensity;  $Q$  and  $U$  provide information about the intensity of linearly-polarized light, at  $0^\circ$  and  $90^\circ$ , respectively; and lastly,  $V$ , accounts for the intensity of circularly polarized light.

Excellent polarimetric sensitivity and spectral resolution are wasted if the optical capabilities of the instrument are not up to par. The design of these instruments must achieve diffraction-limited imaging, with a signal-to-noise ratio ensuring a polarimetric sensitivity of 1000 (typically), and the best spatial resolution the telescope allows, all without sacrificing spectral resolution and accomplishing this in the shortest possible time.

When designing the instrument, one must balance these three properties: spectral, optical, and polarimetric capabilities, trying to improve the performance in all of them without sacrificing too much. In the following sections, we will delve into each of these aspects in more detail.

### 2.1.1 Spectroscopy

Narrow-band tunable spectrographs play a significant role in this thesis. They will be extensively discussed in this chapter, particularly in relation to the design and calibration of TuMag, and again in Chapter 3 when addressing the correction of data produced by these instruments. Therefore, for the sake of simplicity, we will focus exclusively on this type of spectrographs from this point onward.

Fabry-Pérot Interferometers (FPIs), also known as etalons (used interchangeably), represent one of the most prevalent forms of narrow-band tunable spectrographs. Composed by a resonant optical cavity formed by two distinct optical media, these devices allow only the passage of light with wavelengths corresponding to constructive interference within the cavity.

The transmission profile of an etalon, being produced by an interference phenomenon, is characterized by a series of narrow and periodic transmission peaks. The wavelengths at which this resonance peaks are located, their width, and their separation are determined solely by the physical properties of the etalon. In fact, it is not difficult to demonstrate (Bailén et al., 2019) that a resonant cavity produces a periodic transmission profile, with maxima occurring at a wavelength  $\lambda$  such that:

REVISAR -> VÁLIDO PARA TELECENTRIC??

$$\lambda = \frac{2nd \cos \theta}{m}, \quad (2.1)$$

where  $n$  is the refractive index of the medium inside the cavity,  $d$  is the distance between the mirrors,  $\theta$  is the angle of incidence of the incoming light ray and  $m$  is the interferential order ( $m \in \mathbb{Z}$ ).

With Eq. (2.1) in mind, it is clear that an etalon allows for tuning the wavelengths of the transmission peaks by either changing the distance between the mirrors or by altering the refractive index. Although changing the angle of incidence also results in a wavelength



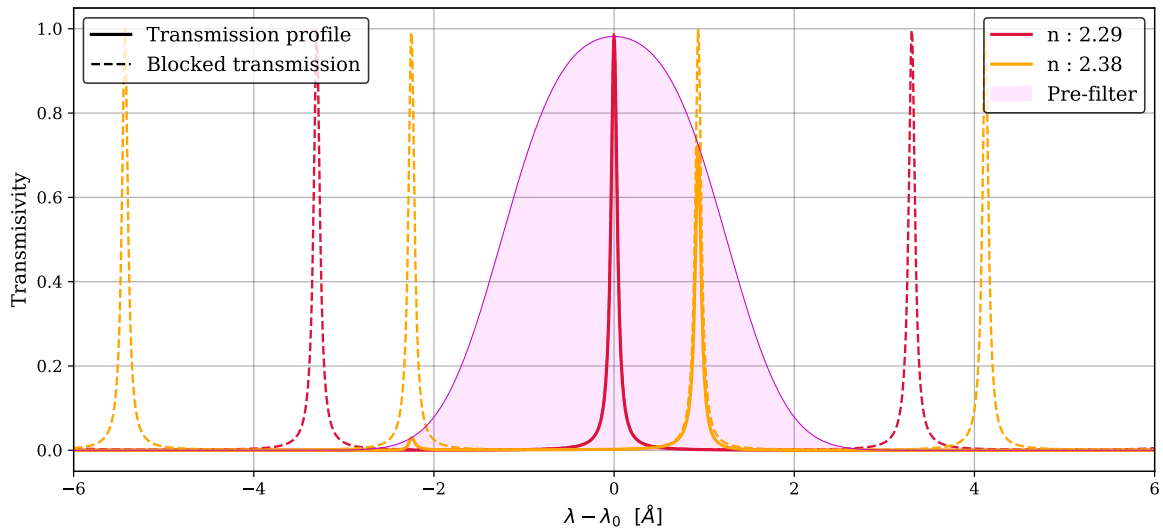


Figure 2.1 Transmission profiles of the same etalon with varying refractive indices ( $n$ ). The dashed lines represent the original transmission profile, while the solid lines indicate the portion of the transmission profile that passes through the order-sorting pre-filter (shaded purple area).

shift, it introduces other issues, such as ghost images or profile broadening in telecentric configurations, among other effects. Consequently, the angle is not used for wavelength tuning.

To tune to a single wavelength (or a very narrow band around it), it is necessary to eliminate the transmission of other peaks. This is typically achieved by using a pre-filter, which only allows light with wavelengths near the desired measurement region to pass through. This ensures that no light reaches the etalon that could pass through it due to interference orders other than the tuned one (secondary orders).

Figure 2.1 shows a simulation of the spectral behavior of this optical setup. The order-sorting pre-filter is shown with a shaded purple area and the unaltered transmission profile of the etalon is shown in dashed lines for different values of the refractive index. In solid lines, the resulting transmission profile is shown, that is, the transmission allowed through both the pre-filter and etalon at the same time.

In reality, their spectral and optical properties can be quite complex and are influenced not only by their physical properties but also by their optical configuration, whether collimated or telecentric. In Chapter 2, we provide a detailed overview of the differences between these configurations, their spectroscopic and optical effects, and the challenges involved in using these devices for data correction.

### 2.1.2 Imaging

### 2.1.3 Polarimetry

## 2.2 The Tunable magnetograph: TuMag

TuMag is a wavelength-tunable spectropolarimeter capable of probing the line-of-sight velocity ( $v_{\text{los}}$ ) and the vector magnetic field ( $\vec{B}$ ) in the photosphere and the low chromosphere. This means that TuMag must be able to switch between different spectral lines and measure the full stokes vector at each observed wavelength.

TuMag's design and properties are a direct consequence of the scientific purpose for which it has been conceived and its requirements.

### 2.2.1 Optical design and image quality.

### 2.2.2 Spectral capabilities

As a spectrograph, TuMag is able to tune the wavelength of the measurements through a Fabry-Pérot interferometer (FPI), and select between three different spectral lines through the different pre-filters located on the filter wheel.

The FPI, or etalon, is a  $\text{LiNbO}_3$ -based ...

### 2.2.3 Polarimetric capabilities

## 2.3 Calibration of TuMag

## **CHAPTER 3**

---

# **OPERATION AND DATA REDUCTION.**

### **3.1 TuMag's Observation modes and data reduction. Data's pipeline.**



## CHAPTER 4

---

# CHALLENGES IN DATA REDUCTION: ETALON CAVITY MAP.

## 4.1 Cavity map retrieval from flat-field observations

### 4.1.1 One device, two configurations

#### 4.1.1.1 Collimated configuration

Collimated mounts are characterized by having the etalon located at the pupil plane and therefore receive a collimated beam from each point of the observed object. In this setup, light coming from any point of the object will fall upon the same area of the etalon. Consequently, any local defects on the etalon crystals or on the plates' parallelism is averaged all over the clear aperture, thus making the optical quality constant along the FoV. However, the angle of incidence of the light beam varies along the FoV, thus shifting the transmission profile.

The transmission profile for an ideal collimated etalon tuned at wavelength  $\lambda_s$  takes the following form:

$$\Psi^{\lambda_s}(\lambda, \theta) = \frac{1}{1 + F \sin^2 a_s(\lambda, \theta)}, \quad (4.1)$$

where

$$a_s(\lambda, \theta) = \frac{2\pi}{\lambda} n d \cos \theta, \quad (4.2)$$

with the subscript  $s$  indicating that the etalon is tuned at the wavelength  $\lambda_s$ .

The shape of the transmission profile depends on its physical properties. Firstly, the width of the resonance peaks is determined by the parameter  $F$ ,  $F \equiv 4R(1 - R)^{-2}$ , which depends exclusively on the reflectivity  $R$  of its mirrors. Secondly, the spectral behavior of the transmission profile is governed by  $a_s(\lambda, \theta)$ , which is a function of the refractive index of the etalon cavity,  $n$ ; the distance between mirrors,  $d$ ; and the angle of the incident beam,  $\theta$ .

Local defects in the collimated configuration are averaged out, which means that  $d$  and  $n$  respectively represent the mean values of the thickness and refractive index across the

clear aperture of the FPI. Yet, they produce a broadening of the transmission profile and worsen the optical quality of the instrument. The differing angles of incidence over the FoV produce shifts of the transmission that vary quadratically with  $\theta$ .

#### 4.1.1.2 Telecentric configuration

In the telecentric configuration, the etalon is placed very close to an intermediate focal plane, while the pupil is focused at infinity. This way, the etalon is illuminated by cones of rays that are parallel to each other and reach different sections of the interferometer. Local inhomogeneities (defects or cavities) on the etalon produce differences in the transmission profile across the FoV, which are directly mapped into the image plane. This means that the optical response and the transmission profile shift locally on the image sensor.

The transmission profile of the etalon tuned at a wavelength  $\lambda_s$  is, in this case, given by (Bail  n et al., 2021):

$$\Psi^{\lambda_s}(\lambda) = \Re [E(a_s(\lambda, n, d, \theta), b)]^2 + \Im [E(a_s(\lambda, n, d, \theta), b)]^2, \quad (4.3)$$

with  $E(a, b)$  being:

$$E(a, b) = 2\sqrt{\tau} \left\{ \int_0^1 \frac{\varrho \cos(a [1 - b\varrho^2])}{1 + F \sin^2(a [1 - b\varrho^2])} d\varrho + i \frac{1 + R}{1 - R} \int_0^1 \frac{\varrho \sin(a [1 - b\varrho^2])}{1 + F + \sin^2(a [1 - b\varrho^2])} d\varrho \right\}, \quad (4.4)$$

where  $\tau$  is the transmission factor of the etalon at normal incidence,  $\varrho$  is the radial coordinate of the pupil normalized to the pupil radius of the instrument,  $a$  is defined by Eq. (4.2) and  $b$  is given by

$$b = \frac{1}{8(nf\#)^2}. \quad (4.5)$$

This parameter accounts for the contribution of the focal ratio,  $f\#$ , and has an impact on the spectral resolution and the apodization of the pupil as seen from the etalon (Beckers, 1998). Thus, the resolution is now affected by both  $F$  and  $f\#$ , through the parameters  $a$  and  $b$ .

Contrary to the collimated case,  $a$  now has an explicit dependence on the spatial coordinates of the image plane, as  $n$  and  $d$  change from pixel to pixel. These variations compose the "cavity error" of the etalon and need to be corrected when employing telecentric configurations.

## CHAPTER 5

---

# SCIENTIFIC EXPLOITATION.

## 5.1 Persistent Homology in Solar Magnetograms.

### 5.1.1 Persistent Homology

Persistent homology stands out as a prominent technique within the topological data analysis toolkit, primarily for its capacity to capture the shape and distribution information of a dataset. The algorithm is rooted in the mathematical framework of homology groups. In topology, these groups measure the number of  $n$ -dimensional holes in a data set, or in other words, the number of connected components for a  $0^{th}$  dimensional analysis, holes or rings for a  $1^{st}$  dimensional analysis, spherical voids for the  $2^{nd}$  dimensional analysis, and so on.

The primary objective of persistent homology is not only to compute the homology groups of a given dataset but also to study how they vary at different scales. To achieve this, the input data undergoes a process of division into a series of sequential subspaces, with each subspace encompassing the previous one. This sequential process, known as filtration, begins with a starting subspace comprising a single point from the original dataset. Subsequent subspaces are then constructed by incrementally adding points to the previous subspace until the final subspace includes all points of the original dataset.

After the filtration process is performed, persistent homology algorithms shift their focus to analyzing the evolution of topological features across the different subspaces. Specifically, they record the filtration value at which a new feature appears, meaning that it is absent in the previous subspace, and when it disappears, meaning that it is no longer present in the following subspaces. These two events are known as the birth and death of a topological feature, respectively.

In a nutshell, the  $n$ -dimensional persistent homology of a dataset with a given filtration can be described as the aggregation of all  $n$ -dimensional features (homology groups) that were created (birth) and subsequently eliminated (death) during the filtration process (Hensel et al., 2021).

When applying persistent homology on a greyscale image, our focus lies in filtering the data according to the pixel values. Multiple filtering approaches exist, with the most extended ones being sublevel and superlevel filtrations, both based on the concept of thresholding. In these filtrations, the image is cropped to a specific value, forming a subspace that

includes all pixels with values higher than this value in a superlevel filtration, or lower in a sublevel filtration. This cropping value (i.e. the filtration value) is systematically varied from the lowest to the highest values of the image, or vice versa, thus generating a different subspace for each value. As a result, the persistence homology analysis captures and examines the evolution of topological features across different thresholds, enabling insights into the image's structural properties at various scales (Barnes et al., 2021).

A more formal way of defining these filtrations can be done by considering an image as a discrete representation of a function  $f$ , defined over a two-dimensional space  $\mathbb{X}$ , such that:

$$f : \mathbb{X} \longrightarrow \mathbb{R} . \quad (5.1)$$

Let  $\mathbb{S}_\phi$  be the subspace of  $\mathbb{X}$  for a filtration value of  $\phi$ . In such a case, a filtration can be expressed as:

$$\mathbb{X} : \mathbb{S}_{\phi_0} \subset \mathbb{S}_{\phi_1} \subset \mathbb{S}_{\phi_2} \subset \dots \subset \mathbb{X} . \quad (5.2)$$

With this formulation, a topological feature with birth-death coordinates:

$$(B, D) = (\phi_I, \phi_{II}) , \quad (5.3)$$

corresponds to a feature that appears for the first time during the filtration process at the subspace  $\mathbb{S}_{\phi_I}$ , and *persists* until the subspace  $\mathbb{S}_{\phi_{II}}$ , where it ceases to exist.

In a sublevel filtration, each subspace can be expressed as:

$$\mathbb{S}_\phi = f^{-1}((-\infty, \phi]) , \quad (5.4)$$

where  $\phi_0$  is selected as the lowest value for any given pixel and its value is increased until the subspace includes all pixels. On the contrary, in a superlevel filtration, the subspaces can be expressed as:

$$\mathbb{S}_\phi = f^{-1}([\phi, \infty)) , \quad (5.5)$$

where  $\phi_0$  is selected as the highest value for any given pixel and its value is decreased along the filtration.

Various methods exist for representing the information derived from a persistent homology analysis, including Betti numbers, persistence bars, and persistent diagrams (PDs) (Cohen-Steiner et al. 2005, Aktas et al. 2019), among many others. For this study, we will utilize the PDs as our chosen approach due to their straightforward interpretation and extended use. A  $n$ -dimensional PD is a multiset of Birth-Death pairs,  $(B_i, D_j)$ , with multiplicity  $k$ , where each pair measures the number ( $k$ ) of  $n$ -dimensional components that have been born at the filtration subspace  $\mathbb{X}_i$  and died in  $\mathbb{X}_j$ , that is usually represented in a 2D scatter plot.

The process of generating a PD of a greyscale image is as follows. We start by selecting the filtration direction (sublevel or superlevel) and the dimension of the analysis (either 0 or 1). We initialize a threshold as the highest or lowest value from the image, depending on the choice of filtration. We then perform the filtration by systematically adjusting the threshold and creating a binary image for each threshold. This process divides the image into two sets: pixels with values above the threshold and pixels with values below it. The



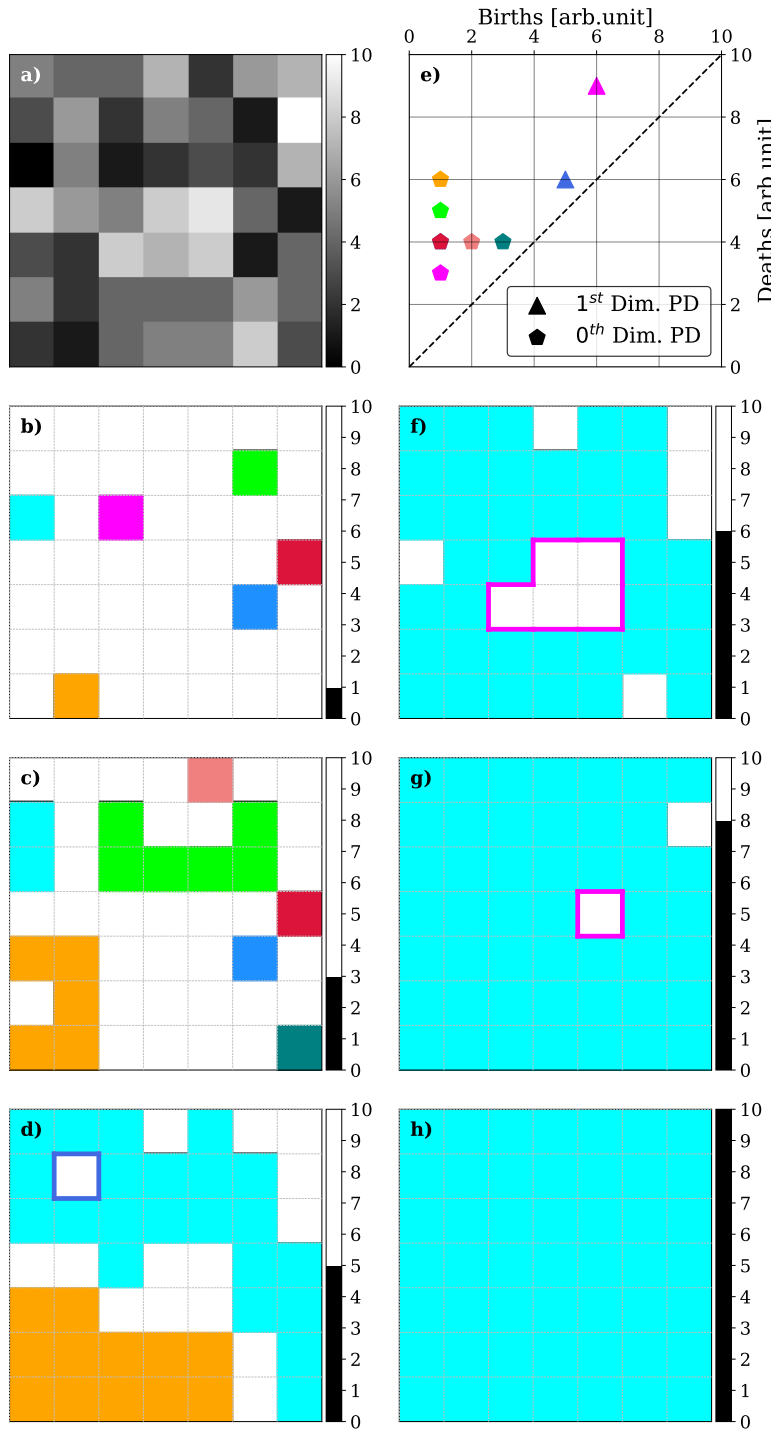


Figure 5.1 Sublevel filtration of a greyscale image and PDs of the  $0^{th}$  and  $1^{st}$  dimensions. Panel a) shows the input data. In panels b), c), d), f), g), and h) different snapshots of the filtration process are shown. The value of the filtration parameter,  $\phi$  is shown in the color bar at the right of each image. Only pixels with a value lower than the filtration value (colored pixels) belong to the subspace shown in each snapshot. Different homology groups are represented with different colors at each snapshot. For connected components ( $0^{th}$  dimensional homology groups) the whole pixel is shown with the corresponding color. For rings, ( $1^{st}$  dimensional homology groups), only the border of each hole is colored. In panel e) the PDs of both dimensions are shown. The color of each point in the diagram is the same as the one used to plot the corresponding topological feature in other panels. An animation depicting the whole filtration process is also provided as part of the article.

choice of filtering determines which of the two sets makes up the subspace. We then look for the existing topological features within each of these subdivisions. The specific process by which these features are identified is detailed in the next paragraph, where the structures corresponding to both dimensions are illustrated using the example shown in Fig. 5.1. We repeat this process until the threshold reaches the opposite limit to that from which it started. Along this process, we follow the appearance, merging, and disappearance of connected components. When two components merge, the longer-lived one (*i.e.* the first to appear along the filtration process) absorbs the younger one, thus resulting in the death of the second (Edelsbrunner & Harer, 2022). We determine the birth and death for each component based on the thresholds at which these events occur. Finally, we construct a scatter plot where the horizontal axis represents the birth values and the vertical axis represents the death values. Each point on this plot corresponds to a persistence point, whose coordinates reveal the scales at which the corresponding topological feature is present.

An example of this process with a sublevel filtration is shown in Fig. 5.1. Panel a) displays the input data, panels b), c), d), f), g), and h) show some of the key steps of the filtration process, and, lastly, panel e) displays the PD for a  $0^{th}$  and  $1^{st}$  dimensional analyses. These plots illustrate how connected components and rings are born and then die as we increase the filtration level. As these components (shown in different colors) increase in size and come into contact with other components, one absorbs the other, thus resulting in the death of the second. This phenomenon is shown in panels b) to d), where we observe the progression of the components until only the blue and orange connected components remain. Additionally, the diagrams also reveal the appearance of two rings in the data (panels f) and g)). These rings are found when pixels that do not belong to the subspace are surrounded by a connected component, and die when those pixels are included in the component as the threshold increases (blue ring in panel f)). Finally, the PD (panel e)) displays the birth and death values (*i.e.* the filtration value) of all the features, of dimensions 0 and 1, that have been identified (birth) and subsequently eliminated (death) throughout the filtration process.

### 5.1.2 Persistent Images

The PD displayed in Fig. 5.1 contains only a limited number of points due to the simplicity of the input image. However, when analyzing real data, these diagrams can consist of hundreds or even thousands of birth-death pairs with high multiplicities, simply due to the size of the images. Additionally, features not only representing the genuine behavior of the data but also reflecting the distribution of noise appear on the diagrams. To address this complexity, several strategies have been developed to simplify the information from PDs, such as persistence curves (Chung & Lawson, 2019), persistence landscapes (Bubenik et al., 2015), or persistence images (PI) (Adams et al., 2017). In this study, we will focus on the latter, due to its noise filtering capabilities and because the representation of the results remains in a Birth-Death diagram, allowing for easy interpretation of the results, similar to a persistence diagram.

PIs are a condensed form of a persistence diagram, offering a concise and easy-to-

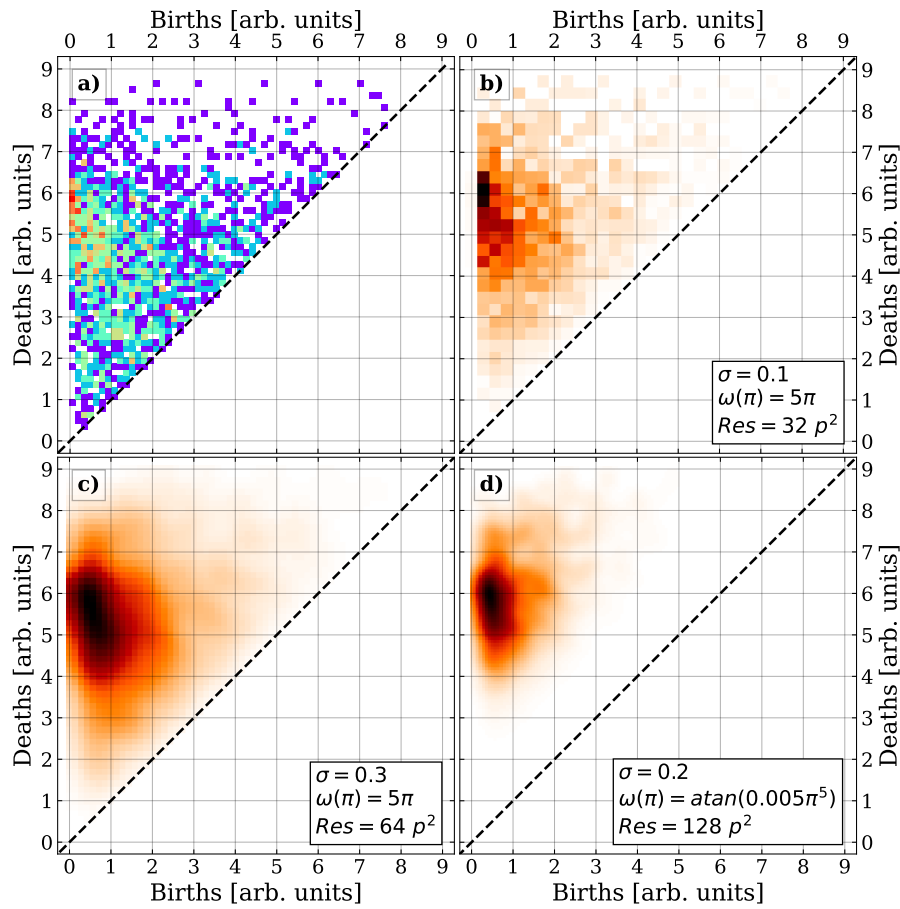


Figure 5.2 Panel a) shows an example of a persistence diagram as a 2D histogram. The color of each bin represents its multiplicity, with the red spots corresponding to higher values. Panels b), c), and d) show three different examples of PIs. The three parameters given in the legends of the PIs are: the standard deviation ( $\sigma$ ) of the Gaussian kernel ( $K(z)$ ), the weighting function, and the resolution of the image PI in pixels ( $p$ ).

understand representation of its topological features. They capture the spatial distribution and persistence information of these features, allowing for the enhancement of the most relevant ones and filtering of the others. A PI is constructed using the concept of persistence. Each topological feature, represented by a point in a PD, has a persistence,  $\pi$ , of:

$$\pi = D - B \quad (5.6)$$

where  $(B, D)$  are the corresponding birth-death coordinates in the diagram. A feature with a large persistence is present at different scales in the data and therefore is more likely to represent the real behavior of the data. On the contrary, short-lived features are typically associated with the noise distribution and usually do not provide much information about the data.

When constructing a PI, a weighting function,  $\omega(\pi)$ , is employed to assign weights to

each point in the diagram, ensuring that longer-lived features have greater weights than shorter-lived ones. There are multiple choices for the shape of the weighting function, which are entirely dependent on the aims of the study and data type. The simplest example is often a linear or power-law relation ( $\omega(\pi) = a\pi^b$ ), where  $a$  and  $b$  can be tuned to assign progressively higher weights to higher persistencies, thus focusing the study on the longer-lived components. On the other hand, if the objective is to filter out noise while assigning similar weights to all non-noise points so that all points have a similar relevance in the analysis, the chosen function is usually an arc-tangent.

The PI is then generated by dividing the persistence diagram plane into a grid with a desired resolution. Within each grid region (or pixel), the weighted features of the diagram within the region are added up using a kernel density estimation. The kernel function,  $K(z)$ , can be tuned to suit the nature and objectives of the analysis, with Gaussian functions being the most common approach.

The resultant PI is a 2D matrix, wherein each pixel corresponds to a specific area in the persistence diagram, and its value represents the cumulative weight of the topological features found within that area. In Figure 5.2, three examples of PI (panels b), c), and d)) are presented for the same persistence diagram (panel a)), where distinct choices of resolution, kernel function, and weighting function have been applied to each image.

All the PDs, PIs, and the rest of the analysis tools presented in this work, have been computed using the Homcloud python package (Obayashi et al., 2022).

### 5.1.3 Data

In this work, we study the results of applying persistent homology to different regimes of solar activity by applying the analysis to both quiet Sun and active region magnetograms.

#### 5.1.3.1 Quiet Sun observations

The study of quiet Sun regions requires high magnetic spatial and temporal resolutions and sensitivities to be able to capture the small-scale evolution of the magnetic structures due to their weak signals and short time scales (Bellot Rubio & Orozco Suárez, 2019). For this reason, we employ observations taken by the Solar Optical Telescope (SOT; Tsuneta et al. 2008) aboard the *Hinode* satellite (Kosugi et al., 2007), a space-borne solar observatory. In particular, we employ observations from *Hinode*'s Operation Plan (HOP) 151. These observations consist of long ( $\geq 20$  h) and mostly uninterrupted sequences of measurements of the Narrowband Filter Imager of the Na I D1 line at 5896 Å taken with a cadence of 50–70 s. The data correction of the selected observation sets has been carried out in (Gošić et al., 2014).

#### 5.1.3.2 Active regions observations

We employ observations of active regions (ARs) taken by the Helioseismic and Magnetic Imager (HMI; Scherrer et al. 2012, Schou et al. 2012) on board the Solar Dynamics Obser-

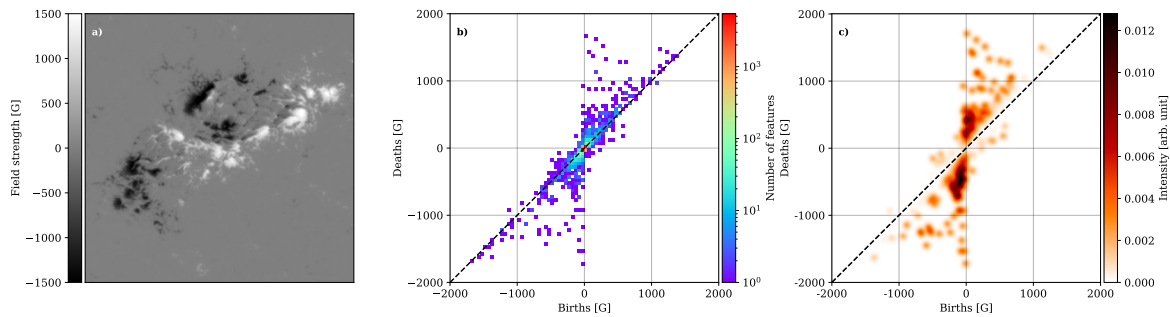


Figure 5.3 (a) SDO/HMI magnetogram taken on 2011-02-13 depicting an active region (NOAA AR 11158). (b) The corresponding PD combining superlevel and sublevel filtrations. (c) PI generated from the PD in panel b) with the following configuration: Resolution = 1000 pixels<sup>2</sup> (4 G per pixel), weighting function:  $\omega(\pi) = \arctan(5 \times 10^{-8}\pi^3)$  and a gaussian kernel with  $\sigma = 40$  G.

vatory (Pesnell et al., 2012). HMI provides a continuous observation of the Sun where a full-disk magnetogram, as well as Dopplergrams, are provided at all times. The full-disk, uninterrupted observations of HMI make it a very suitable instrument to study the evolution of active regions as the formation and development of active regions can be fully captured.

We focus the analysis on a series of newly-emerging ARs identified in (Toriumi et al., 2014a). In particular, we employed the 12-minute cadence observations taken during the period from May 2010 to June 2011, which corresponded to a period of low solar activity.

### 5.1.3.3 Analysis and results

The application of persistent homology to a specific dataset can vary depending on the aims of the study. Different dimensions of the analysis and various types of filtrations focus on distinct features within the data. It is crucial to have prior knowledge of the expected structures and relevant features to be captured in the analysis in order to determine the appropriate approach. In this section, we aim to outline the most appropriate approach for studying the particular case of solar magnetograms.

The solar magnetograms employed here represent the longitudinal component of the magnetic field on the photosphere and are typically presented as greyscale images, as shown in Figure 5.3, panel a). The polarity of the line-of-sight magnetic field is indicated by the sign of each pixel, where positive and negative signals correspond to field lines pointing towards and away from the observer. Applying a single filtration to a greyscale image only displays features corresponding to one polarity (positive or negative) in a PD. However, to conduct a comprehensive study of the magnetic field, both polarities are essential, thus necessitating the use of two separate filtrations with different filtration directions.

We determined that a combination of superlevel and sublevel filtrations with a 1<sup>st</sup>-dimensional persistent homology analysis was the most suitable approach for studying solar magnetograms. This choice is based on two main reasons. Firstly, the 1<sup>st</sup> dimensional

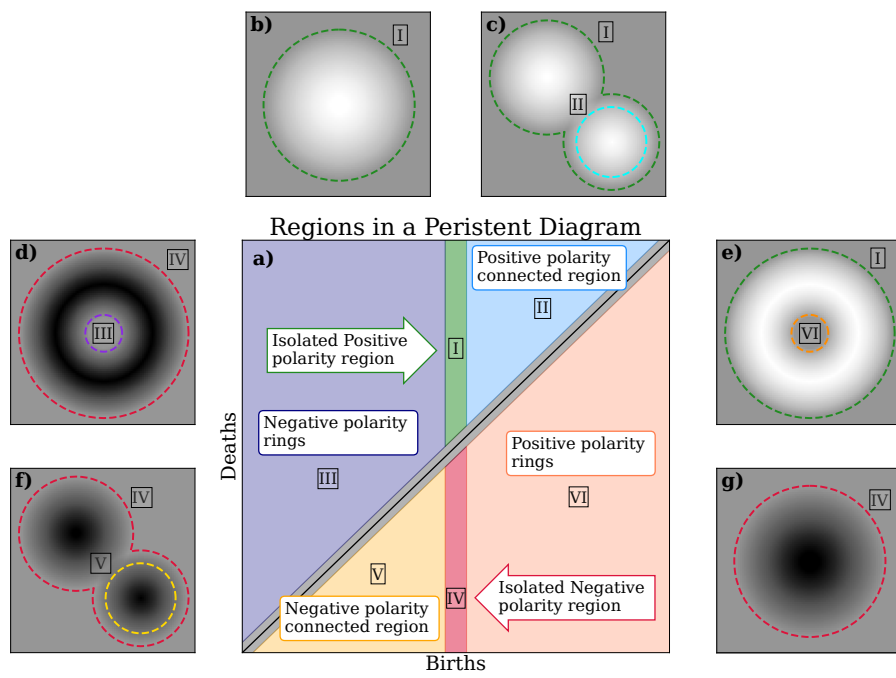


Figure 5.4 Schematic representation of the PD and the different regions (panel a)). The magnetic structures corresponding to the topological features found in the different regions are shown in panels b) to g), with each feature identified by a ring with the corresponding color.

analysis allows us to identify the most prominent features in a PD, which is not the case in the  $0^{th}$  dimensional analysis where the strongest feature does not appear in the diagram as it never dies (see Fig. 5.1). Secondly, by combining superlevel and sublevel filtrations, we can display the results of both filtrations in a single diagram. Features corresponding to different filtrations will have persistencies with opposite signs (features found in a superlevel filtration will be born at higher filtration values than their death, resulting in a negative lifespan). This enables us to construct a PD in which all features displayed above the identity line (with positive persistencies) correspond to the sublevel filtration, and those below the line correspond to the superlevel filtration (see panel b) in Fig. 5.3).

The PDs, and consequently the PIs, offer valuable insights into the magnetic structures present in the magnetograms. The location of a topological feature on the diagram is completely determined by the properties of the corresponding magnetic structure. Specifically, this position is influenced by factors such as the maximum intensity of the magnetic field, its proximity to other magnetic structures, and its geometric shape, including the presence of holes or pores within the structure. These characteristics allow us to partition the diagram into distinct regions, where topological features within each region correspond to different types of magnetic structures.

We distinguished between six distinct regions in the diagram. Figure 5.4 illustrates these regions in panel a) and provides schematic representations of the corresponding magnetic structures in panels b) to g). The regions are as follows: first, topological features located above the identity line (positive persistencies) with birth values close to 0 (region I in the diagram). Features within this region represent isolated magnetic structures of positive polarity, that is, patches of positive magnetic flux fully enclosed by an absence of any magnetic field. The threshold defining what is considered “close to 0” is determined by the data’s properties. To identify isolated structures, we set the threshold as a function of the statistical properties of the background signal (i.e. areas of the magnetogram with little magnetic flux). Specifically, the limits for this region are set as  $(-5\sigma_{bg}, 5\sigma_{bg})$ , where  $\sigma_{bg}$  denotes the standard deviation of the background signal found in a  $15 \times 15$  pixels box devoid of strong magnetic structures.

The second region (II in the diagram) comprises features above the identity line with positive birth values, representing connected structures with positive polarities, that is, positive magnetic field structures in contact with another positive structure but not fully merged. The third region (region III) contains topological features above the identity line with negative birth values, which corresponds to magnetic structures of negative polarity exhibiting a ring-like attribute, namely, structures with pores or holes. These three regions of the diagram have counterparts with negative persistencies. Thus, features associated with isolated structures of negative polarities are found in the region with a birth value close to 0 but below the identity line (region IV), features for connected negative structures are also located below the line but with negative birth values (region V). Lastly, features arising from positive magnetic structures with ring-like attributes are found below the identity line but with positive birth values (region VI).

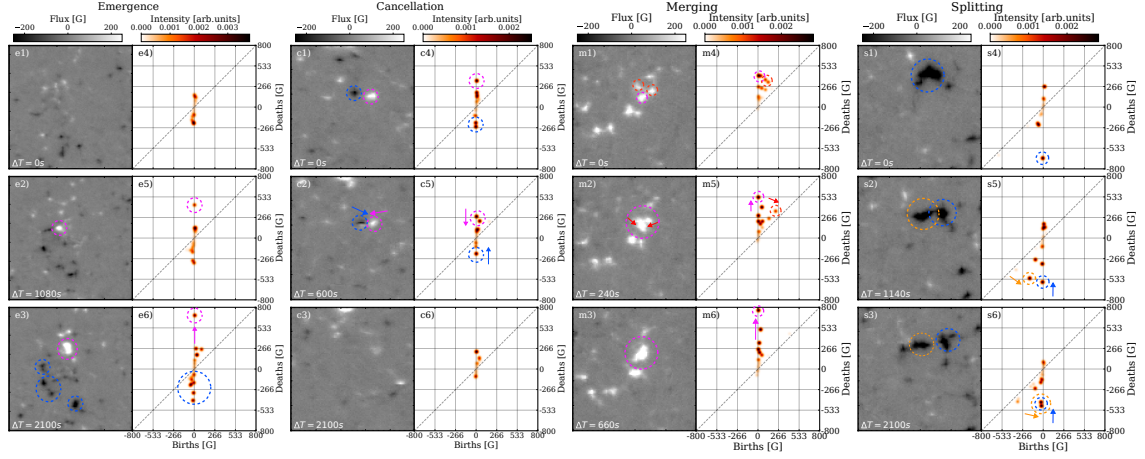


Figure 5.5 Examples of flux emergence (left column), flux cancellation (central left column), merging (central right column), and splitting (right column) events in the quiet sun. The time interval shown in the magnetograms is always with respect to the first frame (panel a) for emergence and g) for cancellation). The PIs correspond to the magnetogram to their left. The parameters for their computation are: resolution = 1000 pixels<sup>2</sup> (1.6 G per pixel), weighting function:  $\omega(\pi) = \arctan(5 \times 10^{-7} \pi^3)$  and a Gaussian kernel with  $\sigma = 16$  G.

#### 5.1.3.4 Quiet Sun results

Quiet Sun regions are characterized by the presence of weak, small-scale magnetic field signals that exhibit rapid evolution. This rapid evolution leads to a multitude of signals in a single snapshot that evolve quickly from one frame to another. The small scale and rapid changes of the processes of the quiet Sun make data analysis techniques desirable for their study due to the complexity of such endeavors.

When examining the evolution of signals across the entire field of view, we observe a dynamic process characterized by numerous regions interacting destructively while new signals emerge throughout the whole region. Despite these continuous changes, the overall structure of the magnetogram appears stable, with consecutive snapshots exhibiting strikingly similar properties. This apparent equilibrium state is also evident when studying the PIs, as consecutive frames show minimal differences in their representations.

Due to the apparent equilibrium state of the overall structure of the magnetograms, it is necessary to narrow down the field to which we apply the analysis. We found that when the number of signals in the studied region is lower, we can observe flux cancellation and emergence events, as well as merging and splitting events, through the changes induced in the persistence diagram. In cancellation events, two regions of magnetic flux with opposite polarities interact destructively, nullifying each other. On the contrary, in flux emergence events, we observe signals of both polarities suddenly emerge from a region with little magnetic flux. In splitting and merging events, only one polarity is involved. Two or more distinct structures of equal polarity merge together in merging events, and a single structure is divided into two or more for splitting events.

In Figure 5.5, an example of an emergence event is shown in three snapshots through



the magnetograms (panels e1 to e3) and their corresponding PIs (panels e4 to e6). When we focus on the second snapshot (panel e2 and e5), we see that a new positive and isolated feature (birth  $\sim 0$ ) that was not present in the previous snapshot has appeared in the PI and stands out from the rest of the signals (highlighted with a pink circle in both magnetogram and PI), while simultaneously, the density of negative polarity features also begins to increase. In the last frame, we see that in the case of positive polarity, the majority of the signal has concentrated in a single structure, as shown by the increase of the death value of the corresponding feature in the PI. A few connected features are also seen, but these are less significant. Meanwhile, the negative polarity signal has been distributed into multiple structures instead of concentrating in a single one, as evidenced by the absence of a prominent feature in the PI and the increased density of connected features (highlighted with blue circles both in the PI and the magnetogram).

A very similar analysis can be carried out to analyze cancellation events. The evolution of the persistence image is very similar to that of the emergence events but in the opposite direction. Figure 5.5 also shows an example of a flux cancellation event through magnetograms (panels c1 to c3) and PIs (panels c4 to c6). In the beginning, the PI shows the presence of features of opposite polarities. When the corresponding structures approach each other and begin to interact, the magnetic signal starts to decrease, which is observed in the PI as a simultaneous movement of the features towards the center of the diagram. This reduction in signal continues until both features reach the center of the diagram, which corresponds to the moment when they will have completely canceled each other out (panels c3 and c6).

For the events that only involve one polarity, namely merging and splitting events, the same behavior is seen in the PI for positive and negative features, but on their respective sides of the PI.

An example of a merging event of positive polarity structures is shown in Fig. 5.5, in panels m1) to m6). These events start with multiple isolated, or interacting structures (as shown in panels m1 and m4), that are moving towards each other. As the structures cluster, two movements are seen in the PI: firstly, the features corresponding to the structures with the weakest field (red features in panels m2 and m5) move towards the identity line; and secondly, the feature corresponding to the main structure (pink feature in panels m2 and m5) experiences an increase in its absolute death value due to the increase in magnetic flux coming from the rest of the structures. When the structures are fully merged, only a single feature appears in both the magnetogram and PI (pink feature in panels m3 and m6), in the isolated region (region I or IV, depending on the polarity).

This process is reversed for splitting events, as shown in panels s1) to s6) of Fig. 5.5. We see how an initially isolated feature in the PI (blue feature in panels s1 and s4) evolves into two (or multiple) features. When the process has started, but the two parts have not yet completely separated, a second feature appears in the diagram in the region corresponding to the connected structures (regions III or V in the diagram), as shown in panels s2) and s5). As the two structures continue to separate, this second feature gradually approaches the region for isolated structures (regions I and IV) as the magnetic field surrounding it in the magnetogram diminishes (panel s5). Eventually, when both structures are completely

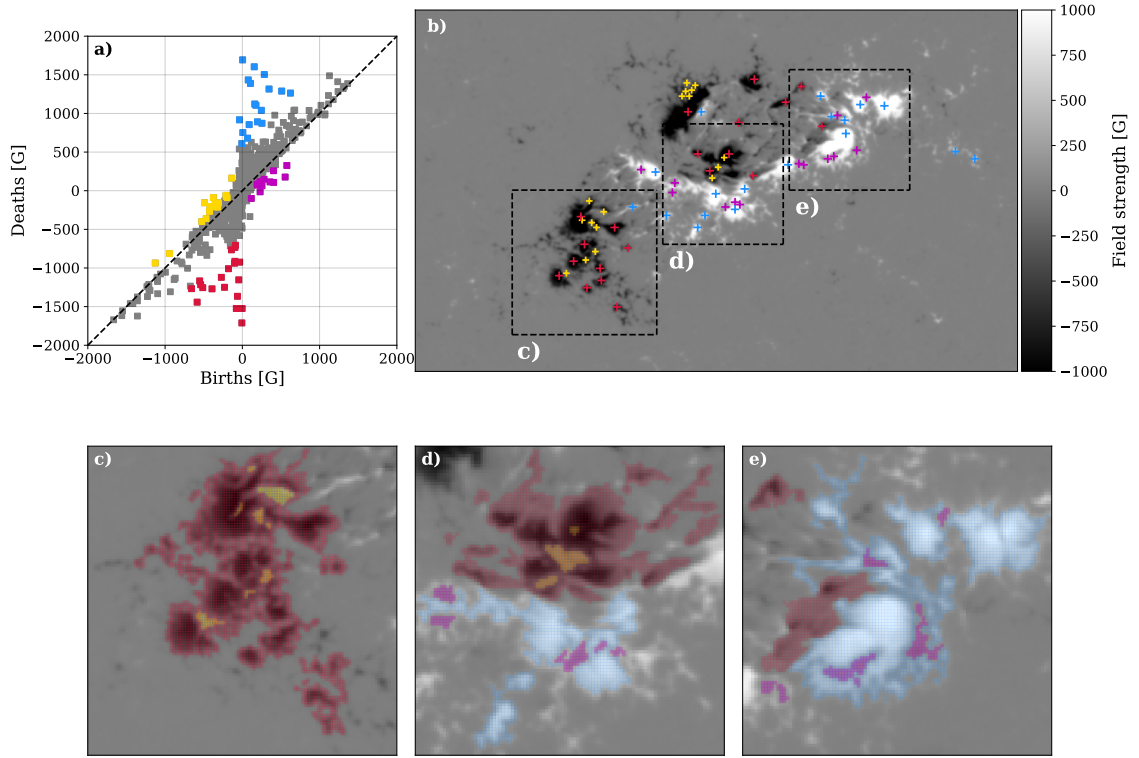


Figure 5.6 SDO/HMI magnetogram taken on 2011-02-13 at 06:34 UT depicting an active region (NOAA AR 11158) and the corresponding persistent diagram (panel a)). Panels c) to e) display a zoomed region of the active region, corresponding to the labeled region with the same letter in panel b). Features of different types are shown in different colors in the diagram. The corresponding structures are shown in the same colors in the magnetograms; as colored crosses in panel b) and as a colored transparent overlay displayed over the whole pixel in panels c) to e) to show the extent of the structure.

separated (i.e. with no signal around them), they will both appear on the diagram as two isolated features with a lower death value compared to the initial one (panels s3 and s5). This reduction occurs because the magnetic flux is distributed between the two structures.

### 5.1.3.5 Active region results

It is important to understand which types of magnetic structures can be identified through persistent homology and establish the correspondence between these structures and the position of the corresponding topological feature in a persistence diagram. To achieve this understanding, Fig. 5.6 displays both a magnetogram with complex morphology (panel b) and its corresponding persistence diagram (panel a), along with three zoomed-in regions of the magnetogram (panels c to e). In all panels, some topological features or their corresponding magnetic structures have been color-coded based on their types, or equivalently, based on their positions in the persistence diagram. In the complete magnetogram (panel

b), structures have been marked with a cross, indicating the pixel where the structure died during the filtration process. Meanwhile, in panels c to e, all pixels composing each structure have been colored. It is noteworthy that nearly all pixels appear colored because we have selected the most significant structures—those with longer lifetimes (Eqn. (5.6)). Consequently, these structures encompass all less significant structures that are absorbed and incorporated into the former during the filtration process.

The analysis of the persistence diagram allows us to deduce several properties of the magnetogram. Firstly, the persistence diagram provides a rapid assessment of the intensity of the magnetic flux since the death value of the topological feature coincides with the maximum flux (in absolute value) within the corresponding structure. In the case of Figure 6, we observe that several structures exhibit maximum (absolute) values surpassing 1500 G, with multiple structures falling within the range of 1000 G to 1500 G.

Secondly, we can infer how the magnetic signals are distributed by examining the number of isolated and connected structures in the diagram (structures highlighted in blue and red depending on their polarity in Fig. 5.6). The complex morphology of the structure displayed in the magnetogram is evident in the high number of connected structures (regions II and V in the diagram) and the absence of prominent isolated structures (regions I and IV).

Lastly, the presence or absence of ring-like structures provides insights into how the magnetic structures are connected. These features can only be found in regions where connected structures create highly complex morphologies with gaps between them, as illustrated in the magnified regions of the magnetogram in Figure 6 (panels c to e).

An example of how the three features allow us to classify ARs depending on their morphologies is shown in Figure 5.7, where three different ARs and their corresponding PIs are displayed. Although at first sight, the PIs appear to be very similar, especially the ones shown in panels d) and f), upon closer inspection, it is possible to find the differences when focusing on the three features mentioned previously. The first AR (panel a)), also shown in Fig. 5.6, shows a very complex morphology, where the magnetic field of both positive and negative polarities is distributed in multiple connected structures. This behavior is displayed in the PI through the high density in the isolated and connected features in equal proportions (i.e. with no prominent features) and with the presence of ring-like features in both polarities. In contrast, the second AR (panel b) shows a simpler magnetic structure with weaker signals. The PI for this case shows an absence of ring-like features in both polarities and a very low density in the regions for connected and isolated features. Lastly, panel c) shows an AR where the positive magnetic field is concentrated in one main area whereas the negative polarity magnetic field shows a fragmented structure. Comparing the corresponding PI with that of the initial case (panels f and d, respectively), a similarity is evident in the region corresponding to negative polarities, observed in both the density of connected components and the presence of ring-type structures. Nevertheless, when examining the positive polarity, it becomes evident that, unlike its negative counterpart, there are only a few prominent isolated structures and a notably low density of connected structures. Furthermore, this asymmetry between the positive and negative distributions is underscored by the absence of ring-like structures in the former.

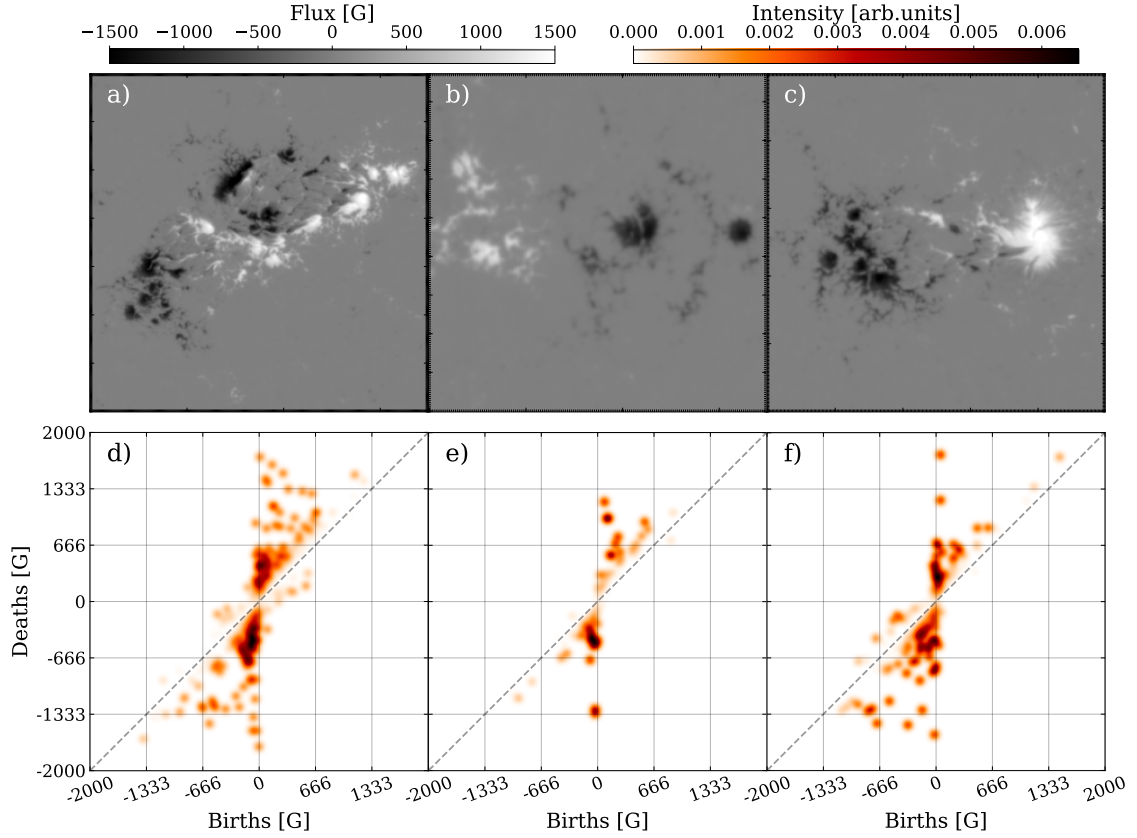


Figure 5.7 SDO/HMI magnetograms of three different active regions and their corresponding persistence images. a) NOAA AR 11158, date: 2011-02-13 at 06:34. b) NOAA AR 11098, date: 2010-08-12 at 20:58. c) NOAA AR 11072, date: 2010-05-22 at 20:58. All persistence images have been generated with the following parameters: Resolution = 1000 pixels<sup>2</sup> (4 G), weighting function:  $\omega(\pi) = \arctan(5 \times 10^{-8} \pi^3)$  and a gaussian kernel with  $\sigma = 40$  G.

### 5.1.3.6 ‘Interacting’ Diagram

So far, we have shown how persistent homology is capable of identifying the various morphologies of active regions and the types of structures that can be identified through persistent images or diagrams. Nevertheless, these structures are either isolated or regions of the same polarity that interact with each other. Due to the nature of the filtration process, persistent homology is unable to detect structures where magnetic fields of opposite polarities form a joint structure. However, ARs where there is a significant interaction between magnetic fields of opposite polarities are of greater interest due to their association with flare production.

This issue is illustrated in the analysis carried out in the previous section of NOAA Active Region 11158 (see Fig. 5.6). Although we can capture the complexity of both positive and negative magnetic structures through the persistent diagram, the  $\delta$ -spots present in the central region remain unnoticed. However, the large number of flare events associated with this region including an X2.2-class event are thought to be related to the abundance of these structures (e.g. Sun et al. 2012, Toriumi et al. 2014b). In this section, we describe a way to efficiently detect and quantify these structures using persistence homology, with only a few additional steps in the analysis.

We start by tracking the position in the magnetogram where rings are detected. Following this, we modify the magnetogram by inverting the sign of one polarity, ensuring that all pixels are either negative or positive. This way, we construct a second ‘magnetogram’ in which we only have information about the intensity, in absolute value, of the magnetic field. This allows us to identify features formed by any combination of signals, whether they are of the same polarity or opposite. Using this new magnetogram, we repeat the analysis and record the positions in the magnetograms at which we find ring-like features. It is worth noting that in this analysis, all the rings identified in the initial step, which were formed by structures of equal polarities, are still detected, although their position in the persistent diagram may have changed due to the change in polarity, hence the relevance of tracking the pixel in the magnetograms. However, only in this second analysis can we identify rings formed between opposite polarities. By selectively considering the ring-like features exclusively identified in this second analysis, we can effectively identify and characterize the structures that are formed by the interaction between different polarities.

Figure 5.8 depicts an example of the interaction analysis for NOAA AR 11158, which exhibits a strong interaction between opposite-polarity fields. Panel a) displays the magnetogram, indicating also the positions where ring-like features have been identified for both positive and negative polarities. Only features with absolute persistencies greater than  $5\sigma_{bg}$  and whose birth occurs in the range:  $(5\sigma_{bg}, \infty)$ , for positive polarities, and:  $(-\infty, -5\sigma_{bg})$  for negative polarities, have been recorded. We now repeat the same analysis but using only the magnitude of the signal. To do this, we invert the positive polarity and, once again, register the positions of the ring-like features in this new magnetogram, as shown in panel b). As observed in panel c), the majority of the interaction rings (*i.e.* those exclusively identified in the second analysis) are located in areas characterized by strong interaction, where the  $\delta$ -spots were found. In these areas, both polarities interact, resulting in the formation of ring-like structures comprising positive and negative magnetic fields due to their close

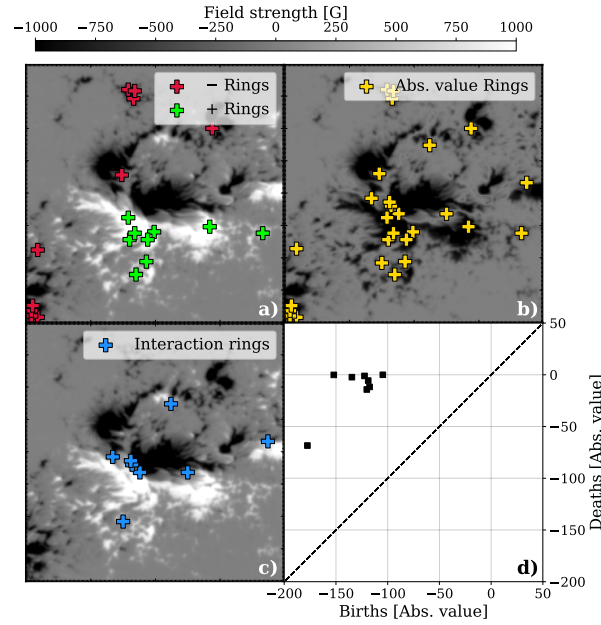


Figure 5.8 Depiction of the different steps carried out for the generation of the interaction diagram (panel d)) for a zoomed-in region of an SDO/HMI magnetogram of NOAA AR 11158 observed on the 2011-02-13 at 18:34. The crosses point to the position at which each of the ring-like structures die, which is always located inside the perimeter of the hole. Panel a) shows the original magnetogram and the position where rings of positive and negative polarities are found. Panel b) shows the magnitude of the field strength in negative values along with the rings found in this representation. Panel c) shows the original magnetogram again, but now featuring the interaction rings, identified when comparing the position of the rings found in the previous steps. Lastly, panel d) shows the ‘interaction diagram’ generated using only the interacting ring structures.

proximity. These areas, such as  $\delta$ -spots, are of particular interest, as they typically harbor magnetic cancellation, reconnection, and flux emergence. However, some points appear to be situated in uni-polar fields. These points, despite what may appear at first sight, are found by this analysis due to a structure that requires the other polarity to close completely and thus form a ring. It is noteworthy that the occurrences of such cases are quite limited when compared to the rings observed in highly interacting zones. While their presence does not necessarily indicate intense interaction, it does imply a certain level of interaction between the two polarities. These features can be represented in a persistence diagram in an analogous way to the standard results of a persistent homology analysis. This is what we have referred to as ‘interacting diagram’ and it is worth noting that only the magnitude of the birth and death coordinates are relevant parameters since the sign will be the one matching the polarity selected at the second step. We have chosen to invert the positive polarity so that these features have positive persistencies, as it is more common in persistent homology studies. However, it is important to emphasize that this decision is completely arbitrary and has no impact on the results of the analysis.

It is useful to determine the information conveyed by the interaction diagram regarding the structures themselves. By taking into account the position and quantity of the interaction rings, along with the temporal evolution of the diagram, we can discern the moment and location where these highly interacting structures develop. Therefore, interaction diagrams could be a new tool to identify, through their topological properties, the strong-gradient polarity inversion lines that characterize  $\delta$ -spots. To achieve this, it is necessary to incorporate into the analysis the temporal evolution of these structures and study the properties that can be extracted from the  $\delta$ -spots through these diagrams, which goes beyond the scope of this work but represents the next (necessary) step to assess the predicting capabilities of persistent homology in the field of solar physics.

### 5.1.3.7 Conclusions

In this study, we investigate the most adequate approach for the application of persistent homology algorithms to the analysis of solar magnetograms. By combining different filtrations in a single one-dimensional persistent homology analysis, we can effectively capture structures corresponding to both polarities of the magnetic field. We have applied this analysis to observations of the quiet Sun and active regions, taken with both Hinode/SOT and SDO/HMI, respectively. Lastly, we have analyzed the results and identified the features of the data that can be found through persistent diagrams and images, and also show some examples of applications of the algorithms.

Our proposed approach to persistent homology algorithms involves the integration of sublevel and superlevel filtrations within a single analysis, enabling the creation of a comprehensive persistence diagram that encompasses features from both positive and negative magnetic structures. Through the examination of the positions of these identified features within the resulting persistence diagram, we can discern the diverse magnetic features present in the magnetograms. This approach has demonstrated its efficacy in capturing the intricate complexity of magnetic structures, with a particular emphasis on active regions. Through this method, we have achieved successful differentiation between the vari-

ous morphologies present in active regions by analyzing the presence or absence of specific features in the corresponding persistence images.

On the other hand, the persistent images obtained from quiet Sun observations exhibit significant similarity to each other. This indicates a lack of overall evolution in the magnetic structures within these regions. In quiet Sun areas, small regions of magnetic flux interact with each other in small-scale events, while the overall structure remains relatively static. These small-scale events become more apparent in persistent images when the field of view is reduced. These small-scale events, such as flux emergence or cancellation, can be observed through persistent images as a joint movement of negative and positive features. In cancellation events, the features move toward the center of the image, while in emergence events, they move away from the center.

Additionally, we have successfully identified interactions between opposite-polarity magnetic fields by detecting ring-like features formed by these two polarities. To achieve this, we introduced a method for calculating an ‘interaction diagram’ that selectively displays features resulting from the interaction between polarities. This interaction diagram is generated by comparing the ring-like features identified in an analysis using only the absolute value of the signal with those found in the standard analysis. This approach enables us to detect the presence of  $\delta$ -spots and quantify the level of interaction between polarities, which is one of the critical factors for the understanding and prediction of flare eruptions.

In conclusion, our application of persistent homology to solar magnetograms has provided a comprehensive and insightful framework for studying magnetic structures on the solar surface. The topological features derived from magnetograms serve as a foundation for classifying active regions based on their morphology and level of interaction, as certain topological features may have inherent connections to solar atmospheric phenomena. For instance, the presence of interaction rings in active regions might be correlated with flare production, while the interaction of signals from opposite polarities observed in a persistent diagram in the quiet Sun could be linked to small-scale reconnection events or the separation of signals associated with flux emergence. The exploration of these relationships and the assessment of the presented tools in achieving precise active region classification and their potential as predictive tools are topics of our upcoming research. Moreover, we have introduced new tools, such as the interaction diagram, which facilitates the detection and quantification of structures interacting with opposite polarities, like  $\delta$ -spots, addressing a crucial aspect of flare prediction. The findings presented in this article lay a solid foundation for future studies, emphasizing the potential of persistence images as valuable inputs for machine learning algorithms and contributing to advancements in space weather forecasting.

Lastly, it is important to emphasize that in this study we have focused primarily on static images in order to provide a solid basis for future investigations. The next logical step in this study is to complete the analysis of active regions, which includes examining their temporal evolution. This approach allows for the simultaneous consideration of two key factors in understanding flare eruption processes: morphological complexity, whose analysis is intrinsic to persistent homology, and the study of their temporal evolution through the analysis of the evolution of persistence and interaction diagrams.



## CHAPTER 6

---

# SUMMARY AND CONCLUSIONS

The conclusions are ...



## APPENDIX A

---

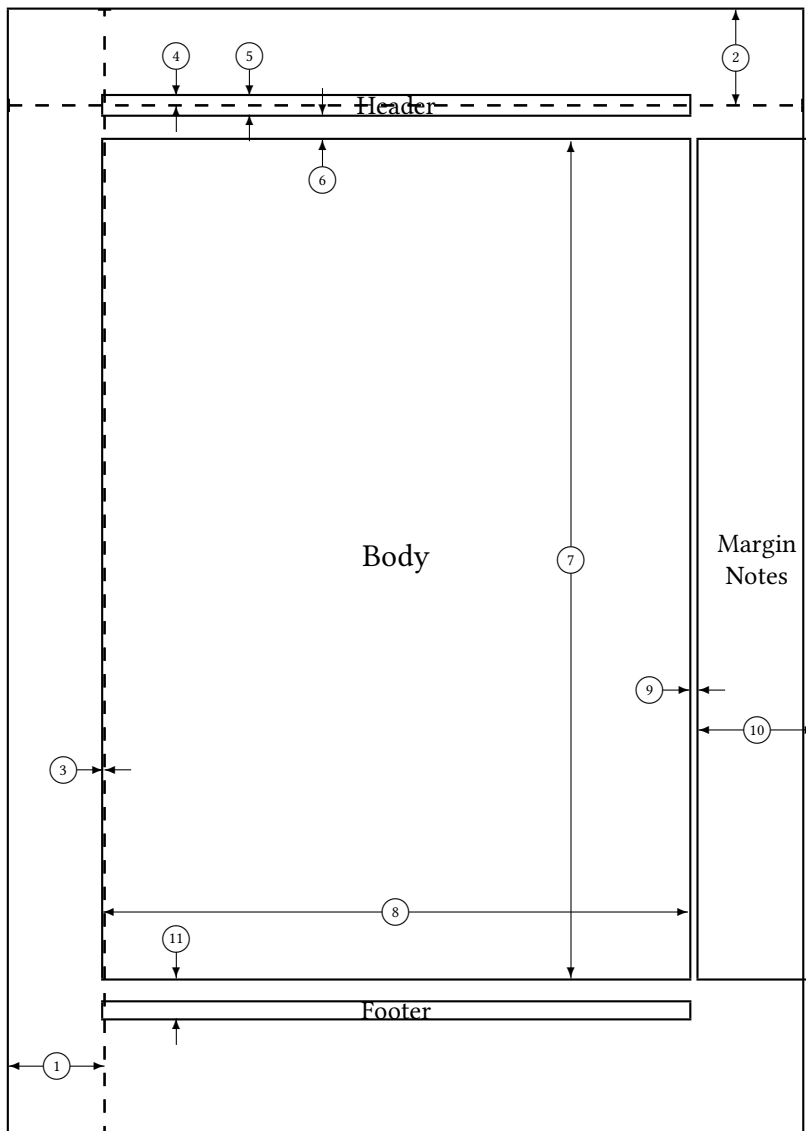
### PROFILE DERIVATIVES



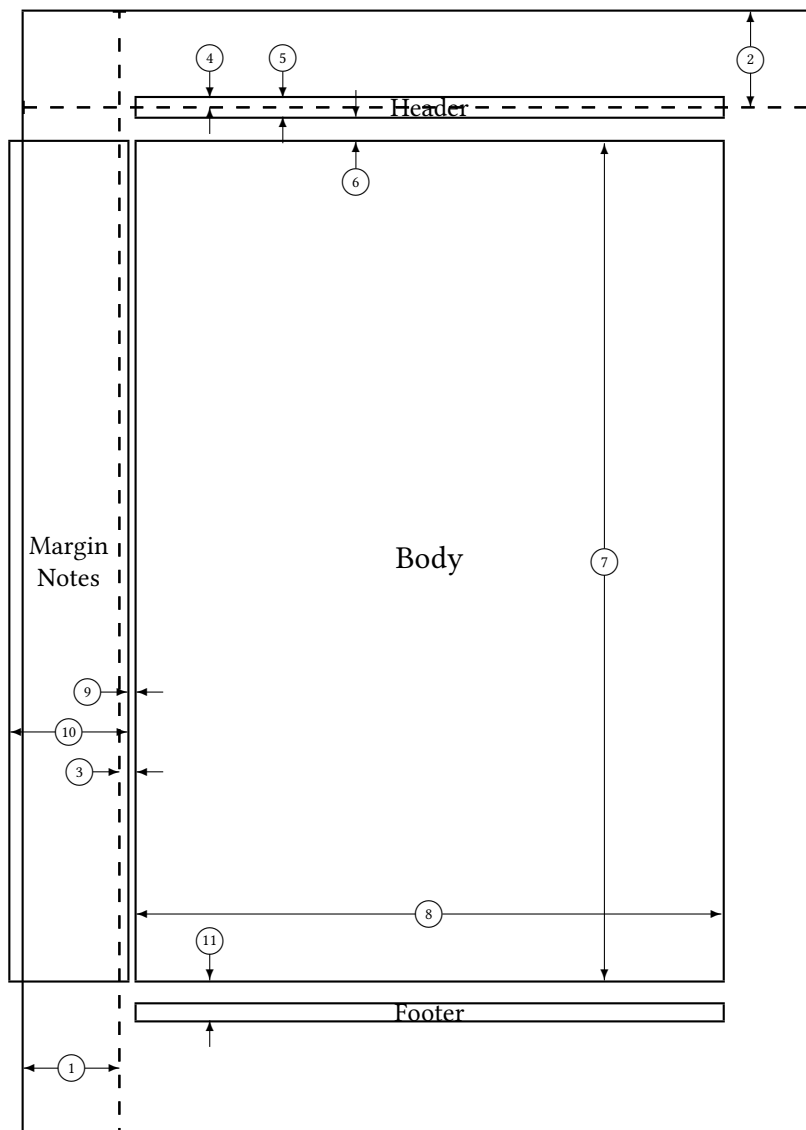
# BIBLIOGRAPHY

- Adams, H., Emerson, T., Kirby, M., et al. Persistence images: A stable vector representation of persistent homology. *Journal of Machine Learning Research* **18**, 1 (2017).
- Aktas, M. E., Akbas, E., & Fatmaoui, A. E. Persistence homology of networks: methods and applications. *Applied Network Science* **4**, 1 (2019).
- Bailén, F. J., Suárez, D. O., & del Toro Iniesta, J. On fabry–pérot etalon-based instruments. i. the isotropic case. *The Astrophysical Journal Supplement Series* **241**, 9 (2019).
- Bailén, F. J., Suárez, D. O., & del Toro Iniesta, J. On fabry–pérot etalon-based instruments. iv. analytical formulation of telecentric etalons. *The Astrophysical Journal Supplement Series* **254**, 18 (2021).
- Barnes, D., Polanco, L., & Perea, J. A. A comparative study of machine learning methods for persistence diagrams. *Frontiers in Artificial Intelligence* **4**, 681174 (2021).
- Barthol, P., Gandorfer, A., Solanki, S. K., et al. The sunrise mission. *Solar Physics* **268**, 1 (2011).
- Beckers, J. On the effect of narrow-band filters on the diffraction limited resolution of astronomical telescopes. *Astronomy and Astrophysics Supplement Series* **129**, 191 (1998).
- Bellot Rubio, L., & Orozco Suárez, D. Quiet sun magnetic fields: an observational view. *Living Reviews in Solar Physics* **16**, 1 (2019).
- Bubenik, P., et al. Statistical topological data analysis using persistence landscapes. *J. Mach. Learn. Res.* **16**, 77 (2015).
- Chung, Y., & Lawson, A. Persistence curves: a canonical framework for summarizing persistence diagrams. arxiv. *arXiv preprint arXiv:1904.07768* (2019).
- Cohen-Steiner, D., Edelsbrunner, H., & Harer, J. Stability of persistence diagrams. *Proceedings of the twenty-first annual symposium on Computational geometry*, 263–271 (2005).
- Edelsbrunner, H., & Harer, J. L. (2022), *Computational topology: an introduction* (American Mathematical Society).

- Gošić, M., Rubio, L. B., Suárez, D. O., Katsukawa, Y., & del Toro Iniesta, J. The solar inter-network. i. contribution to the network magnetic flux. *The Astrophysical Journal* **797**, 49 (2014).
- Hensel, F., Moor, M., & Rieck, B. A survey of topological machine learning methods. *Frontiers in Artificial Intelligence* **4**, 681108 (2021).
- Kosugi, T., Matsuzaki, K., Sakao, T., et al. The hinode (solar-b) mission: An overview. *Solar Physics* **1**, 3 (2007).
- Obayashi, I., Nakamura, T., & Hiraoka, Y. Persistent homology analysis for materials research and persistent homology software: Homcloud. *journal of the physical society of japan* **91**, 091013 (2022).
- Pesnell, W., Thompson, B., & Chamberlin, P. The solar dynamics observatory (sdo). *Solar Physics* **275** (2012).
- Scherrer, P. H., Schou, J., Bush, R., et al. The helioseismic and magnetic imager (hmi) investigation for the solar dynamics observatory (sdo). *Solar Physics* **275**, 207 (2012).
- Schou, J., Scherrer, P. H., Bush, R. I., et al. Design and ground calibration of the helioseismic and magnetic imager (hmi) instrument on the solar dynamics observatory (sdo). *Solar Physics* **275**, 229 (2012).
- Solanki, S., Riethmüller, T., Barthol, P., et al. The second flight of the sunrise balloon-borne solar observatory: overview of instrument updates, the flight, the data, and first results. *The Astrophysical Journal Supplement Series* **229**, 2 (2017).
- Stokes, G. G. On the composition and resolution of streams of polarized light from different sources. *Transactions of the Cambridge Philosophical Society* **9**, 399 (1851).
- Sun, X., Hoeksema, J. T., Liu, Y., et al. Evolution of magnetic field and energy in a major eruptive active region based on sdo/hmi observation. *The Astrophysical Journal* **748**, 77 (2012).
- Toriumi, S., Hayashi, K., & Yokoyama, T. Statistical analysis of the horizontal divergent flow in emerging solar active regions. *The Astrophysical Journal* **794**, 19 (2014).
- Toriumi, S., Iida, Y., Kusano, K., Bamba, Y., & Imada, S. Formation of a flare-productive active region: observation and numerical simulation of noaa ar 11158. *Solar Physics* **289**, 3351 (2014).
- Tsuneta, S., Ichimoto, K., Katsukawa, Y., et al. The solar optical telescope for the hinode mission: an overview. *Solar Physics* **249**, 167 (2008).



- |    |                       |    |                                  |
|----|-----------------------|----|----------------------------------|
| 1  | one inch + \hoffset   | 2  | one inch + \voffset              |
| 3  | \oddsidemargin = -1pt | 4  | \topmargin = -7pt                |
| 5  | \headheight = 14pt    | 6  | \headsep = 19pt                  |
| 7  | \textheight = 631pt   | 8  | \textwidth = 441pt               |
| 9  | \marginparsep = 7pt   | 10 | \marginparwidth = 88pt           |
| 11 | \footskip = 30pt      |    | \marginparpush = 7pt (not shown) |
|    | \hoffset = 0pt        |    | \voffset = 0pt                   |
|    | \paperwidth = 597pt   |    | \paperheight = 845pt             |



- |    |                                     |    |   |
|----|-------------------------------------|----|---|
| 1  | <code>one inch + \hoffset</code>    | 2  | <code>one inch + \voffset</code>              |
| 3  | <code>\evensidemargin = 13pt</code> | 4  | <code>\topmargin = -7pt</code>                |
| 5  | <code>\headheight = 14pt</code>     | 6  | <code>\headsep = 19pt</code>                  |
| 7  | <code>\textheight = 631pt</code>    | 8  | <code>\textwidth = 441pt</code>               |
| 9  | <code>\marginparsep = 7pt</code>    | 10 | <code>\marginparwidth = 88pt</code>           |
| 11 | <code>\footskip = 30pt</code>       |    | <code>\marginparpush = 7pt (not shown)</code> |
|    | <code>\hoffset = 0pt</code>         |    | <code>\voffset = 0pt</code>                   |
|    | <code>\paperwidth = 597pt</code>    |    | <code>\paperheight = 845pt</code>             |